

# Experimentally-validated mesoscale modeling of the coupled mechanical-thermal response of AP-HTPB energetic material under dynamic loading

Ruize Hu<sup>1</sup>, Chandra Prakash<sup>2</sup>, Vikas Tomar<sup>2</sup>, Michael Harr<sup>2</sup>,  
Ibrahim Emre Gunduz<sup>3</sup>, and Caglar Oskay<sup>\*1</sup>

<sup>1</sup>*Department of Civil and Environmental Engineering  
Vanderbilt University, Nashville, TN 37235, USA*

<sup>2</sup>*School of Aeronautics and Astronautics  
Purdue University, West Lafayette, IN 47907, USA*

<sup>3</sup>*School of Mechanical Engineering  
Purdue University, West Lafayette, IN 47907, USA*

## Abstract

This manuscript presents a combined computational-experimental study of the mesoscale thermo-mechanical behavior of the Hydroxyl-terminated polybutadiene (HTPB) bonded ammonium perchlorate (AP) composite energetic material subjected to dynamic loading conditions. The computational model considers the AP-HTPB interface debonding, post-debonding interface friction and temperature rise due to viscoelastic dissipation as well as dissipative interfacial processes. The interface is modeled using a cohesive zone model combined with a contact algorithm to account for the interface separation, particle/binder contact and heat generation. The HTPB binder is modeled as viscoelastic with adiabatic temperature rise. Three experiments are conducted to calibrate and validate the model. Raman spectroscopy and indentation experiment are employed to determine the interface properties, whereas Kolsky bar tension test along with in-situ synchrotron x-ray diffraction measurements are used

---

\*Corresponding author address: VU Station B#351831, 2301 Vanderbilt Place, Nashville, TN 37235. Email: caglar.oskay@vanderbilt.edu

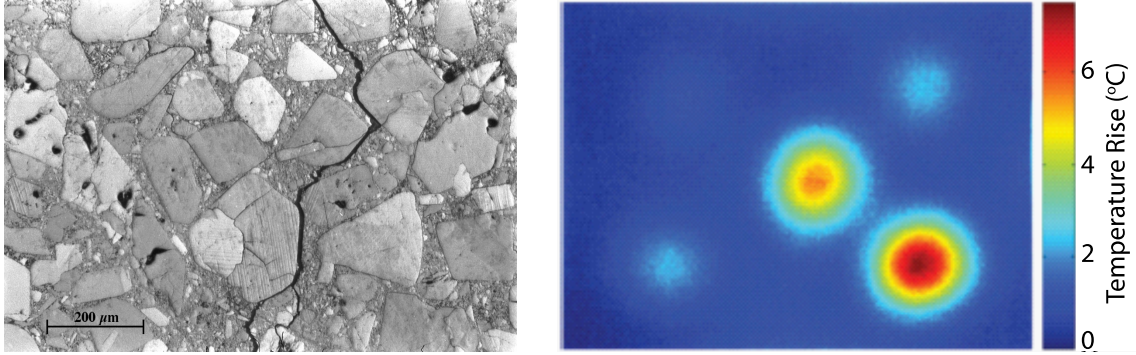


Figure 1: Interface debonding and frictional heating. (a) Optical micrograph of the post failure route in PBX 9501 [44] (reprinted with permission from JSTOR). (b) Localized temperature rise at interface [32] (reprinted with permission from AIP Publishing).

to validate the model and understand the interface separation characteristics under dynamic loading.

*Keywords:* Energetic material; Interface modeling; Raman spectroscopy; Kolsky bar; Cohesive zone model

## 1 Introduction

Polymer-bonded explosives (PBXs) are particulate composites with very high volume fraction of energetic particles embedded in a polymeric binder. The thermo-mechanical behavior of PBXs or PBX constituents subjected to static and dynamic loads has been investigated in the past few decades (e.g., [44, 45, 8, 51, 31, 7, 17, 63, 11]). The mechanical and thermo-mechanical response of PBXs have been shown to be sensitive to the properties of the interfaces between the particles and the binder [44, 45, 53, 17, 32]. Debonding sites initiated at interfaces extend through the polymeric binder, coalesce and ultimately result in mesoscopic and macroscopic cracks as shown in Fig. 1a. Furthermore, the particle/binder interface, upon debonding, leads to temperature rise induced by frictional heating as shown in Fig. 1b. Together with the heating induced by dissipation within the binder and the inelastic (e.g. fracture, plastic) processes within the particles as well as particle-particle interfaces, the particle binder interface constitutes one of the causes of hot-spot formation in PBXs even in the absence of shock.

While there are extensive studies of the properties of polymeric binders [33, 14], and polycrystalline explosive particles [34, 6] or the overall composites [50, 8, 44, 45], the particle/binder interface has not yet been well characterized due to the difficulty in direct measurement and characterization of the interface properties. Experimental studies with scanning electron microscope (SEM) by Rae et al. [44, 45] and Zhou et al. [69] suggest that the dominant failure mechanism in PBXs is particle/binder interface debonding in quasi-static loading conditions. It is observed that cracks initiate and propagate along the interface of the large filler particles and the binder. This observation points to the need to devise interface damage models to investigate the failure mechanisms in PBXs. Using digital image correlation technique applied to a macroscopic fracture experiment, Tan et al. [53] proposed a microscopic cohesive law of PBX 9501. The cohesive traction-separation relation is derived in a homogenized sense based on the extended Mori-Tanaka method. Wu and Huang [63], and Barua and Zhou [10] employed cohesive zone models to simulate the progressive debonding of particle/binder interface in PBX 9501. Despite the mesoscale description of the interface behavior, these investigations could only be validated against macroscopic variables (e.g., bulk stress-strain) due to the lack of direct experimental measurements at the mesoscale.

A majority of the hot spot generation mechanisms are attributed to mechanically induced localized heating subjected to dynamic loads [20]. Mares et al. [31, 32] and Miller et al. [35] investigated heating due to the viscoelastic binder and frictional heating at particle/binder interface with ultrasonic excitation. Dienes et al. [17] and Barua and Zhou [10] investigated the effect of frictional heating at the interfaces due to sliding. In addition, heating mechanisms within crystal particles such as, void collapse, jetting and dislocation pile-up avalanche were investigated by Baer [7], Barton et al. [9], and Armstrong et al. [4, 5], respectively. The direct effect of heating is not only on detonation, but also physical changes such as melting, phase transition and material property changes due to the temperature dependent binder and particle behaviors. The temperature dependent macroscopic response of PBXs is reported in [21, 8, 51].

In this manuscript, an experimentally validated mesoscale interface model for AP-HTPB material system is proposed, accounting for interface debonding and frictional heating. The

particle/binder interface debonding is modeled using a cohesive zone model. A viscoelastic constitutive model is used for the HTPB binder. Frictional heating at the particle/binder interface and heating due to viscous dissipation within the HTPB binder are modeled. The unique contribution of this work is that the key cohesive interface model parameters (i.e. interface fracture energy, strength and stiffness) are directly measured from the Raman spectroscopy and indentation experiments, and the model performance is validated by direct experimental observations.

The remainder of this manuscript is organized as follows: Section 2 describes the experimental procedures for measuring the material properties for model calibration, as well as the experimental setup for model validation and response investigation. Section 3 presents the formulation of the HTPB model and the thermo-mechanical cohesive zone model for the particle/binder interface. Section 4 provides the details of the model calibration process. Section 5 presents the simulation results compared to the experimental observations and discussions. Section 6 provides the conclusions and future research directions.

## 2 Experimental procedures

### 2.1 Sample preparation

The samples consist of ammonium perchlorate (AP) particles embedded in hydroxyl-terminated polybutadiene (HTPB). AP particles obtained from Firefox had a nominal diameter of 600  $\mu\text{m}$ . Spherical particles in the range 600-800  $\mu\text{m}$  were manually selected. HTPB was fabricated using a mixture of R-45M liquid polybutadiene (Firefox) and isophorone diisocyanate (IPDI) at an OH index ratio of 1.05. Additionally, a surface binding agent (Tepanol) was added at a mass ratio of 0.5 to fabricate samples with higher surface adhesion, while keeping the same index ratio. The constituents were manually mixed and degassed in vacuum for 30 minutes. They were poured into PTFE molds with a depth of 1 mm and the particles were added. The samples were cured at 60° C in a convection oven for 10 days. After the cure, they were removed from the molds and cut into appropriate shapes for testing.

## 2.2 Nanoindentation

In this work, the properties of AP-HTPB interfaces are probed by nanoscale impact experiments. Nano-indentation techniques have been successfully applied to model the site specific behavior such as at the interface between two materials at high strain rates [57]. The novelty of the experiments lies in the fact that impacts are precisely at the interfaces in the precision range of nanometers to micrometers as required by the material microstructure. The probe used for indentation has tip radius of 1  $\mu\text{m}$ . This tip impacts at the interfaces thus making sure that energy from the impact is delivered at the interfacial region. The dynamic indentations were performed using the high strain rate impact schedule of Micro Materials, UK [56, 57, 58, 59]. The experimental setup consists of the 3D stage to mount the sample that allows it to move in three orthogonal directions. The indents were performed with a spherical indenter. The indenter is mounted on a pendulum that is hanging vertically on frictionless springs to let it move freely. The force on the pendulum is applied through the electromagnets. The depth of indents is measured as function of change in the capacitance of the plates attached at the back of the indenter. The additional force for high strain rate impacts is provided with the help of a solenoid placed at the lower part of the pendulum. From its initial stationary solenoid position, the indenter position is monitored continuously as a function of time, including the initial impact trajectory and the initial rebound from the material surface [59]. The velocity of the indenter can be calculated as the first derivative of the depth-time response. The maximum depth ( $h_{max}$ ), the initial contact velocity ( $V_{in}$ ), the outgoing velocity ( $V_{out}$ ), the residual depth ( $h_{res}$ ) are calculated from this data. The residual depth is the position at the point of detachment from the sample on the first rebound. The strain rate,  $\dot{\epsilon}$ , of the impact changes with the depth of impact. An average strain rate characterizing the impact can be approximated as:

$$\dot{\epsilon} \approx \frac{V_{in}}{h_{max}} \quad (1)$$

where,  $h_{max}$  is the maximum depth and  $V_{in}$  is the maximum velocity. The strain and stress are given by:

$$\epsilon = \frac{h_{res}^2}{h_{max}^2}; \quad \sigma = \frac{P}{\pi h_{max}^2} \quad (2)$$

The strain rate in the current dynamic indentation experiment depends on the maximum applied impact load.

## 2.3 Raman spectroscopy

Micro-Raman spectroscopy is a technique of measuring stress at meso and microscales. Raman spectroscopy is concerned with the phenomenon of the change of frequency when light is scattered by molecules. If the frequency of the incident light is  $\nu_o$  and that of a component of the scattered light is  $\nu_r$ , then the frequency shift,  $\nu_r - \nu_o = \Delta\nu$ , may be either positive or negative. Its magnitude is referred to as Raman frequency. The set of Raman frequencies of the scattering species constitutes its Raman spectrum. The Raman frequencies are independent of the exciting frequency  $\nu_o$  and are characteristic of the species giving rise to the scattering. Raman shifts are equivalent to the energy changes involved in transitions of the scattering species and are therefore characteristic of them. Raman shifts are typically reported in wavenumbers, as wavenumbers are related to energy. The first experimental investigation of the effect of external stress on the Raman modes was done by Anastassakis et al. [3] on silicon. Raman scattering measurements in the presence of externally applied stress have been previously performed [16].

Several studies involving Raman spectroscopy of AP and Polybutadiene have been reported in the literature [13, 15, 19, 29, 36, 37, 43, 60]. The pressure dependence of internal mode frequency in AP was studied by Brill and Caetz [12], who reported that as the pressure increases, the Raman shift of internal mode frequency of  $\text{NH}_4^+$  and  $\text{ClO}_4^-$  both increase. However the N-H stretching mode Raman shift decreases with increase in pressure [29]. The temperature dependence of Raman active modes in the single crystal AP has also been investigated [15]. Nallasamy et al. [36] analyzed the Raman and Infra-Red spectra of cis- and trans-1, 4-polybutadiene and assigned the vibration modes to the observed frequency. Fell et al. [19] used the Fourier transform Raman spectroscopy to characterize different samples of energetic materials and propellant formulations. Raman spectra of several energetic materials were measured to be in the range of 100 to 3000  $\text{cm}^{-1}$ .

In the current study, a HORIBA Xplora Plus micro-Raman spectrometer was used to

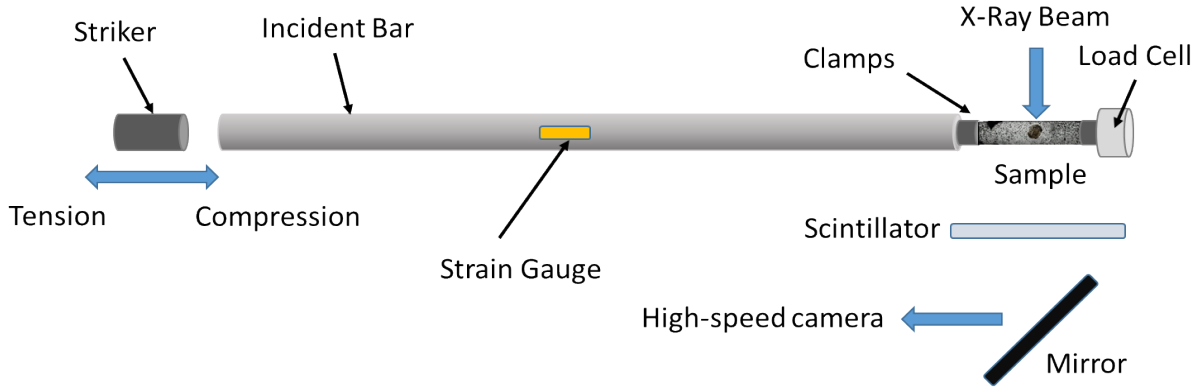


Figure 2: Schematic of the Kolsky bar setup.

obtain the Raman spectra at an excitation wavelength of 532 nm and a grating size of 2400. The resolution of the micro-Raman spectrometer is  $1.4 \text{ cm}^{-1}$ . A Deben loading stage was used to load the sample at a rate of 0.1 mm/min until failure.

## 2.4 Kolsky bar with Phase Contrast Imaging

The dynamic high strain-rate (1000/s) delamination of ammonium perchlorate particles in an HTPB binder was investigated at Argonne National Laboratories at the beamline 32-ID-B using phase contrast imaging on a miniature Kolsky bar apparatus. Kolsky bar testing involves the application of a mechanical pulse to a sample delivered through two long stainless steel bars at a predetermined loading rate. The striker can push or pull on the bar to generate compression or tension in the sample. Traditionally, the incident and transmitted waves are measured using strain gauges to determine loading rate and forces. Due to space constraints at the experimental hutch, the transmission bar was replaced with a load cell to measure the dynamic stresses and strains in the material. The schematic of the experimental setup is shown in Fig. 2. Further details of the setup are described previously [41, 24]. The phase contrast imaging was performed using synchrotron radiation produced from the undulator which was filtered to produce the pink beam—a narrow spectral band of electron energies. The method relies on the difference in the x-ray absorptivity of materials, where heavier elements have larger absorptivities. The energy was selected to give good contrast between the particle and the binder. The undulator spacing was set to vary the x-ray flux to prevent damaging the sample

and the imaging equipment. The beam was sent through the sample and the transmitted x-rays were converted to photons using a scintillator (Al<sub>5</sub>Lu<sub>3</sub>O<sub>12</sub>: Ce). The luminescence was imaged using a high speed camera (Kirana, Specialised Imaging) operated at 50,000 frames per second. The imaging window size was approximately 2 x 2 mm with 640 x 480 pixels. The sample dimensions were 6 x 2 x 1 mm and they were clamped from the two ends within a width of 2 mm. The sample holder was attached to the load cell and pre-strained to a certain amount between 0.2 to 0.6 by moving the load cell. This was done so that the debonding would occur within the imaging window, because of the high compliance of the HTPB binder. Due to the length of the bar, a displacement of 600  $\mu$ m could be applied per wave transmission. Since the binder is very compliant, the bar stop was spaced enough to allow multiple steps of bar bulk motion, which enabled larger total extension. The load traces were measured using an oscilloscope attached to a Kistler charge amplifier connected to the load cell.

### 3 Model formulation

The simulation of the dynamic response of the AP-HTPB energetic composite requires constitutive models for each constituent, i.e., the particle, binder and the interface. Within the appropriate load regime, the AP particle is assumed to behave elastically. The constitutive models that idealize the behavior of the binder and the interface are described below.

#### 3.1 HTPB model

The constitutive behavior of the HTPB binder is idealized as viscoelastic with strain rate and temperature dependency. Previous investigations on the dynamic behavior of polymer composite matrix including HTPB also employed viscoelastic models to describe its behavior [64, 33]. We employ the viscoelastic constitutive law originally proposed by Amirkhizi et al. [2], which has been used in the investigation of the dissipative response of polymeric composites subjected to high rate loading [25].

The Cauchy stress tensor is expressed in terms of the hereditary integral as a function of

the shear relaxation modulus as:

$$\boldsymbol{\sigma} = \int_0^t 2G(t, \tau) \mathbf{D}'(\tau) d\tau + K \frac{\ln J}{J} \boldsymbol{\delta} \quad (3)$$

where,  $\mathbf{D}'(t)$  is the deviatoric component of the deformation-rate tensor,  $\mathbf{D} = (\mathbf{L}^T + \mathbf{L})/2$ , with  $\mathbf{L}$  the velocity gradient tensor ( $\mathbf{L} = \dot{\mathbf{F}}\mathbf{F}^{-1}$ ),  $\mathbf{F}$  the deformation gradient tensor and  $G(t, \tau)$  the shear relaxation modulus. The volumetric part of the deformation is taken to behave elastically and  $K$  is the elastic bulk modulus.  $J$  is the determinant of the deformation gradient, and  $\boldsymbol{\delta}$  the Kronecker delta.

The shear relaxation modulus,  $G(t, \tau)$ , is idealized using the Prony series representation:

$$G(t, \tau) = \frac{T(\tau)}{T_{\text{ref}}} G_{h\infty} \left( 1 + \sum_{i=1}^n p_i \exp \left( \frac{-(\xi(t) - \xi(\tau))}{q_i} \right) \right) \quad (4)$$

where,  $G_{h\infty}$  is the steady-state shear modulus of HTPB,  $T$  the temperature,  $T_{\text{ref}}$  is the reference temperature,  $p_i$  and  $q_i$  are the fitting parameters of the Prony series prescribing the relative modulus and the relaxation time of the  $i$ th Prony series term, respectively.

$$\xi(t) = \int_0^t \frac{1}{a(T(\tau))} d\tau \quad (5)$$

where  $a(T)$  is the Williams-Landel-Ferry (WLF) empirical time-temperature shift function:

$$\log(a(T)) = \frac{A(T - T_{\text{ref}})}{B + T - T_{\text{ref}}} \quad (6)$$

$A$  and  $B$  are material parameters.

In the context of high rate loading driven by relatively quick heat generation through viscoelastic dissipative process within HTPB, and in view of relatively low conductivity and short loading time window, adiabatic conditions are assumed. We note that slower loading regimes (e.g. creep damage [18]) for the same material could require coupled treatment of heat conduction and mechanical deformation. The adiabatic heating induced by viscoelastic

dissipation is expressed as:

$$\dot{T} = \frac{1}{C_{Vh}} \dot{W}_d = \frac{2G_{h\infty}}{C_{Vh}} \frac{T(t)}{T_{\text{ref}}} \sum_{i=1}^n \frac{p_i}{q_i} \boldsymbol{\varepsilon}_d^i(t) : \boldsymbol{\varepsilon}_d^i(t) \quad (7)$$

where  $W_d$  is the dissipated work per unit reference volume,  $C_{Vh}$  the heat capacity per original volume, and a superposed dot indicates material time derivative.

$$\boldsymbol{\varepsilon}_d^i(t) = \int_0^t \exp\left(\frac{-(\xi(t) - \xi(\tau))}{q_i}\right) \mathbf{D}'(\tau) d\tau \quad (8)$$

Equation 7 implies that the entire mechanical dissipation contributes to the generation of heat and none stored within the material through irreversible deformation mechanisms. While it is possible to consider a portion of the dissipation for heat generation [1], quantification of the apportionment is not straightforward and not employed in this study.

### 3.2 Interface model

The interface between the particles and the binder plays an important role in the macroscopic mechanical and thermal response of energetic materials. On one hand, the debonding and crack propagation along the particle interface is a dominant failure mode [44, 45]. On the other, the friction between the particles and the binder material is one of the heat sources that contributes to hot-spot formation [31, 32, 46]. A thermo-mechanical cohesive zone model is employed to model the progressive debonding at the particle/binder interface, and the heating caused by post-debonding friction. The traction-separation relation of the cohesive zone model is based on a bilinear law proposed by Tomar et al. [54]. We employ the combined measure of displacement jump proposed by Tvergaard and Hutchinson [55]:

$$\lambda = \begin{cases} \sqrt{\left(\frac{\Delta_n}{\Delta_{nc}}\right)^2 + \left(\frac{\Delta_t}{\Delta_{tc}}\right)^2}, & \Delta_n \geq 0 \\ \frac{|\Delta_t|}{\Delta_{tc}}, & \Delta_n < 0 \end{cases} \quad (9)$$

where  $\Delta_n$  and  $\Delta_t$  denote the normal and tangential separations in the normal and tangential directions, respectively (see Fig. 3(b)), whereas  $\Delta_{nc}$  and  $\Delta_{tc}$  are the corresponding critical

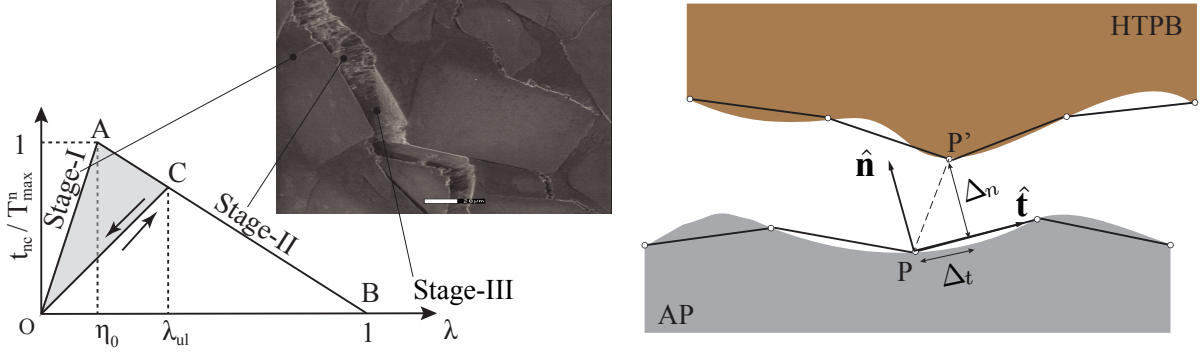


Figure 3: (a) Bilinear cohesive law. The micrograph is from [44] and reprinted with the permission of JSTOR. (b) Schematic illustration of interface separation.

separations. The cohesive strength vanishes, and the particle and binder completely debonds when the pure normal separation reaches  $\Delta_{nc}$ , and when the pure shear separation reaches  $\Delta_{tc}$ .

The bilinear cohesive law is defined in three stages. In Stage-I, the interface is undamaged and the traction-separation relationship is linear until  $\lambda = \eta_0$  ( $\eta_0$  is the elastic separation limit). Interface damage initiates in Stage-II, featured by the softening of cohesive strength as the separation increases. The maximum separation the interface has experienced up to an arbitrary time instance  $t$  is defined as:

$$\lambda_{ul} = \max_{\tau \in [0, t]} \{\lambda(\tau)\} \quad (10)$$

any unloading and reloading with separation less than  $\lambda_{ul}$  linearly unload and reload (path OC in Fig. 3(a)) with reduced cohesive stiffness. As the separation further increases to 1, the interface damage state enters Stage-III, i.e. fully damaged, featured by the vanished cohesive traction. Based on the characteristics of the bilinear cohesive law, the damage parameter  $d$  is defined as:

$$d = \begin{cases} 0, & 0 \leq \lambda_{ul} \leq \eta_0 \quad (\text{Stage-I}) \\ \frac{\lambda_{ul} - \eta_0}{(1 - \eta_0)\lambda_{ul}}, & \eta_0 < \lambda_{ul} \leq 1 \quad (\text{Stage-II}) \\ 1, & \lambda_{ul} > 1 \quad (\text{Stage-III}) \end{cases} \quad (11)$$

The cohesive fracture energy within the cohesive zone is expressed as:

$$\Phi_0 = \Phi_{re} + \Phi_d \quad (12)$$

where,  $\Phi_d$  is the dissipated energy due to the fracture process, and  $\Phi_{re}$  is the residual cohesive energy stored at the interface, which is expressed as a function of the damage variable:

$$\Phi_{re} = \Phi_0(1 - d) \frac{\lambda_m}{\eta_0} \quad (13)$$

where,  $\lambda_m = \max\{\lambda_{ul}, \eta_0\}$ .  $\Phi_d$  corresponds to energy dissipation during the decohesion process alone and does not account for the frictional dissipation further described below. In the present formulation, the fracture energy is taken to be invariant of the path of separation (i.e., the fracture energy under pure mode I and mode II loads are the same), i.e.,:

$$\Phi_0 = \frac{1}{2} T_{max}^n \Delta_{nc} = \frac{1}{2} T_{max}^t \Delta_{tc} \quad (14)$$

where  $T_{max}^t = \alpha T_{max}^n$  and  $\alpha = \Delta_{nc}/\Delta_{tc}$  is a material parameter.  $T_{max}^n$  and  $T_{max}^t$  are the mode I and mode II interface cohesive strengths, respectively. This approximation has been previously employed successfully to study the behavior of ceramic composite materials [65] and PBX 9501 [10]. The cohesive potential energy at any separation state  $\lambda$  is then written as:

$$\Phi = \frac{\lambda^2}{\lambda_m} \Phi_{re} \quad (15)$$

By differentiating the cohesive potential energy with respect to the normal and tangential separations, respectively, the traction components are obtained as:

$$t_{nc} = (1 - d) \frac{T_{max}^n}{\eta_0} \frac{\Delta_n}{\Delta_{nc}} \quad (16)$$

$$t_{tc} = (1 - d) \frac{T_{max}^t}{\eta_0} \frac{\Delta_t}{\Delta_{tc}} \quad (17)$$

The interpenetration at the particle/binder interface subjected to compressive loading is

accounted for using a contact algorithm [61]. Impenetrability is imposed based on the penalty method. Considering a linear relation between interpenetration (  $|\Delta_n|$  ) and penalty traction,  $p_n$ :

$$p_n = \beta |\Delta_n| H(-\Delta_n) \quad (18)$$

where,  $\beta$  is the penalty parameter, and  $H$  the Heaviside function. The tangential traction exists in both stick and slip modes. Due to the non-differentiability of Coulomb law at the transition between these two modes, a regularized Coulomb law [61] is employed as an approximation to the classical Coulomb law:

$$t_{tf} = \mu \frac{\dot{\Delta}_t}{\sqrt{\dot{\Delta}_t^2 + \varepsilon^2}} |p_n| \quad (19)$$

where  $\varepsilon$  is a constant regularization parameter and as it approaches zero, the expression recovers the classical Coulomb law.  $\mu$  is the friction coefficient that is assumed to be a function of damage parameter to account for the friction due to the slip between the particle and binder cohesive surfaces in partially damaged stage:

$$\mu = d \mu_0 \quad (20)$$

where  $\mu_0$  is the friction coefficient when the cohesive surfaces are fully separated but in contact.

Combining the cohesive and the contact behavior, the local normal and tangential tractions are expressed as:

$$\mathbf{t}_n = [H(\Delta_n)t_{nc} + (H(\Delta_n) - 1)p_n]\hat{\mathbf{n}} \quad (21)$$

$$\mathbf{t}_t = [t_{tc} + (1 - H(\Delta_n))t_{tf}]\hat{\mathbf{t}} \quad (22)$$

where,  $\hat{\mathbf{n}}$  and  $\hat{\mathbf{t}}$  are respectively the normal and tangential unit vectors to the interface in local coordinate system.

The frictional work done by the separated cohesive surfaces is considered as the major dissipation mechanism at interface. The work done during the decohesion process that is converted to heat is taken to be negligible compared to the frictional heating. The dissipated energy at interface induces localized temperature rise under the adiabatic assumption. The

total energy dissipation rate is computed as:

$$\dot{Q} = \dot{Q}_f = t_{tf} \dot{\Delta}_t \quad (23)$$

The temperature rise at the interface is then computed as:

$$\dot{T}_{int} = \frac{\dot{Q}}{C_{Vint}} \quad (24)$$

where  $C_{Vint}$  is the volumetric specific heat capacity of the interface.

In view of the temperature- and rate-dependent binder properties, the interface behavior is likely to exhibit rate- and temperature-sensitivity as well. Rate-sensitive cohesive formulations have been previously proposed [63, 22, 70, 68, 47]. It is critical to establish not only model formulations, but also experimental calibration and validation procedures that carefully probe rate effects on the interfacial behavior. Such combined experimental-computational developments are ongoing and will be employed in the future.

### 3.3 Model implementation

The models for the AP-HTPB material system are implemented using the user defined subroutine capabilities of the commercial finite element program, Abaqus. Within the framework of the explicit solver of Abaqus, the HTPB model was implemented using VUMAT—user defined constitutive law. For efficiency, the numerical evaluation of the hereditary integral in Eq. 3 is performed by the recurrence relationship, as detailed in [49]. The cohesive zone model along with the contact algorithm is implemented using VUEL—user defined element. The cohesive zone element implementation follows the formulation of the PPR model proposed by Paulino and co-workers [42]. Contact conditions are imposed on the pair of cohesive surfaces of the cohesive zone elements and activated when interpenetration is detected. This approximation of contact behavior at particle/binder interface is accurate when the sliding motion between the cohesive surfaces remains relatively small.

All numerical simulations described in calibration, validation and sensitivity studies employ

three-noded constant strain elements in the discretization of particle and binder domains.

## 4 Model calibration

Model calibration includes the identification of the material properties for the HTPB binder, the AP particles, as well as the cohesive law parameters for the interface model. The calibration is conducted based on the experimental data from Raman spectroscopy, indentation experiment as well as the experimental data available in the literature.

### 4.1 Calibration of phase properties

The material properties of HTPB show significant dependence on temperature and strain rate [14]. The mechanical behavior of HTPB is primarily viscoelastic at or near room temperature. Near the glass transition temperature (i.e. 208K), elastic-viscoplastic behavior becomes pronounced. The density of HTPB ( $\rho_h$ ) is 0.95 g/mm<sup>3</sup>. The specific heat capacity per unit volume,  $C_{Vh} = 1.987$  mJ/mm<sup>3</sup>K [23].

The viscoelastic parameters (i.e., the Prony series parameters and temperature dependence) were calibrated based on the experiments performed by [14]. The experimental data spanning approximately 6 orders of magnitude in loading rate and 50° K in temperature have been employed. We note that experiments have been performed at high rate or quasi-static state, and intermediate rates of strain have not been experimentally probed. Setting the reference temperature as 253° K, the Prony series parameters and temperature sensitivity parameters are calibrated. The stress-strain curves of the calibrated model compared to the experimental data [14] are shown in Fig. 4 and the corresponding parameters are provided in Table 1. The parameter calibration is performed through optimization, where the discrepancy between the stress-strain behavior computed by the simulation and provided by the experiments is minimized.

The quasi-static elastic modulus was experimentally observed to be 2.5 MPa, which is consistent with previously reported values (Cady et al. [14] recorded 2.01 MPa) for similar HTPBs. Experimental data on the Poisson's ratio of HTPB is not available to the authors,

Table 1: HTPB model parameters.

$G_{h\infty}$ [MPa]	$\nu_h$	$\rho_h$ [g/mm <sup>3</sup> ]	$C_h$ [mJ/mm <sup>3</sup> K]	T [K]
0.948	0.45	$0.95 \times 10^{-3}$	1.987	296
$p_1$	$p_2$	$p_3$	$p_4$	$p_5$
33	30	25	13	8
$p_6$	$q_1$ [ms]	$q_2$ [ms]	$q_3$ [ms]	$q_4$ [ms]
3	$1.04 \times 10^{-7}$	$2.1 \times 10^{-5}$	$1.66 \times 10^{-3}$	0.0105
$q_5$ [ms]	$q_6$ [ms]	A	B	$T_{\text{ref}}$ [K]
0.05	0.21	-15	102	253

and taken to be the same as that of Sylgard 184, which has Poisson’s ratio 0.45 [48, 52].

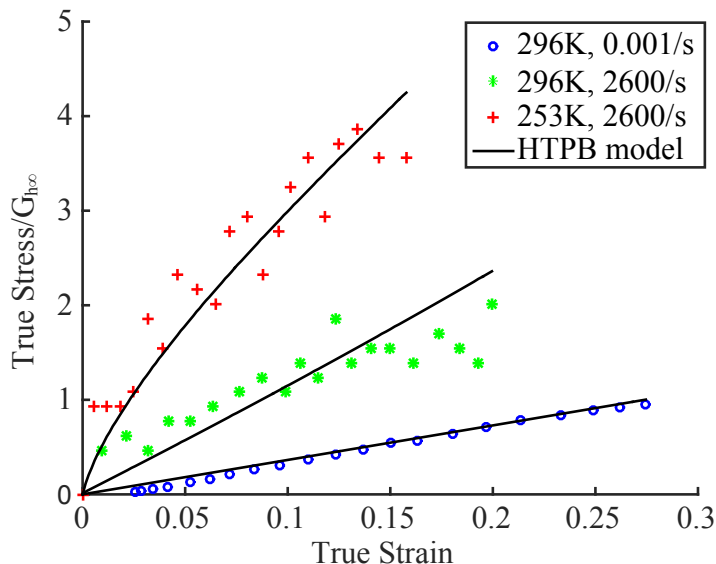


Figure 4: Calibration of the HTPB stress-strain curves.

The material property for AP particle is assumed to be elastic, and the Young’s modulus and Poisson’s ratio is obtained from [30]. The density and volumetric specific heat capacity of ammonium perchlorate are reported by Hanson P. and Parr [23] as  $\rho_a = 1.95 \times 10^{-3}$  g/mm<sup>3</sup> and  $C_{Va} = 2.121$  mJ/mm<sup>3</sup>K, respectively.

## 4.2 Cohesive law calibration

The interface model parameters are obtained from the Raman experiment, the nanoindentation experiment as well as data available in literature [23, 62, 17]. The interface fracture

energy and strength are determined in the Raman experiment. Nanoindentation experiment is performed to extract the stress-strain curve of the interface, through which the interface stiffness is obtained.

The interface width is taken as the average distance between the point within HTPB and the one adjacent within AP, where a clear difference between HTPB and AP could be discerned under the microscope,  $w_{\text{int}} \approx 1 \mu\text{m}$ . The interface density and specific heat capacity is obtained as the average of those of the two phase materials (i.e., HTPB and AP), i.e.,  $\rho_{\text{int}} = 0.5(\rho_a + \rho_h) = 1.45 \times 10^{-3} \text{ kg/mm}^3$  and  $C_{V\text{int}} = 0.5(C_{Va} + C_{Vh}) = 2.054 \text{ mJ/mm}^3\text{K}$ .

The interface fracture energy and strength were obtained using a single edge notched tensile specimen as shown in Fig. 5. The notch was placed in the sample between one edge of the specimen and the interface. In the current study we have applied a uniaxial tensile load and recorded the Raman shift at different loads.

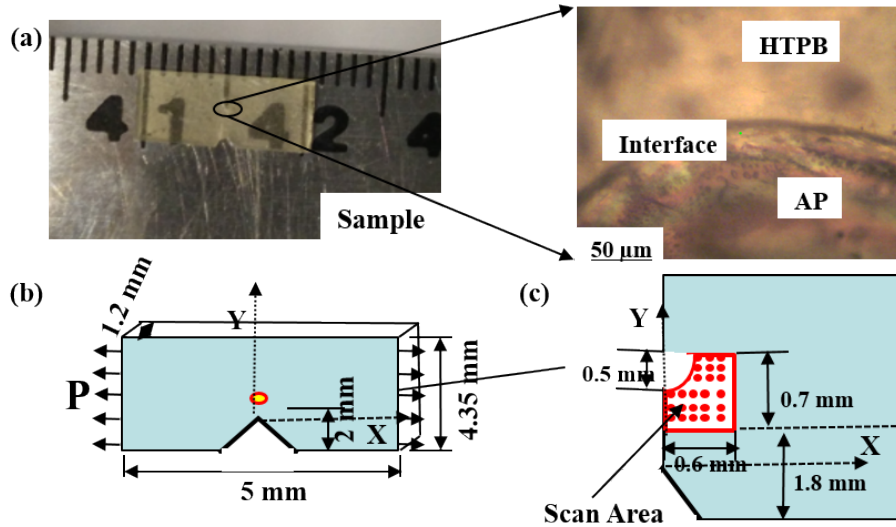


Figure 5: (a) AP-HTPB sample. (b) Boundary conditions for the experiment. (c) Scanned Area.

Raman shifts were observed and recorded near the interface in the scanned area as shown in Fig. 5 in the  $\text{CH}_2$  stretching zone as a function of applied stress. Raman shifts were measured and the shift vs stress at the crack tip was plotted as shown in Fig. 6. The slope of the fitted

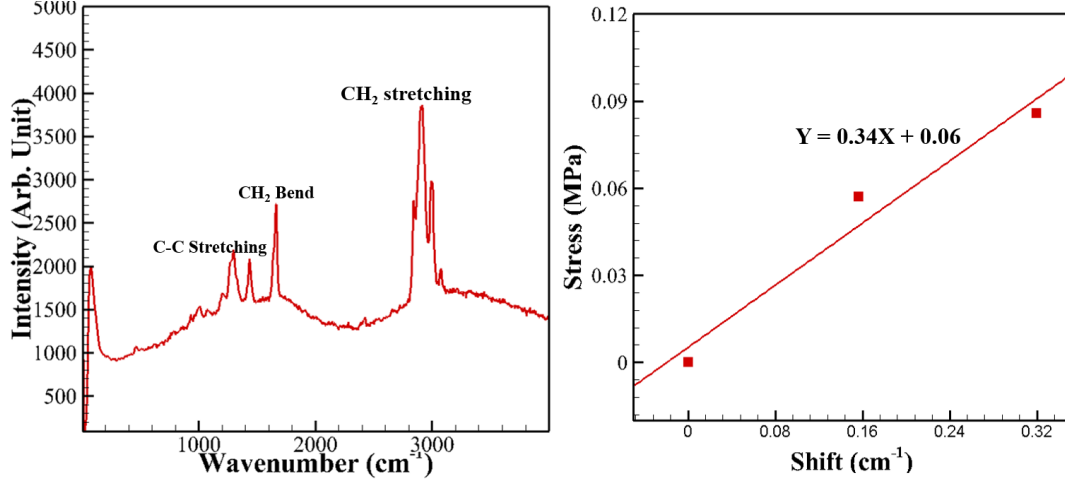


Figure 6: (a) A typical Raman spectra of HTPB. (b) Stress vs wave number shift calibration curve.

line is 0.34 MPa/cm<sup>-1</sup>. Stress in the scanned area was then calculated using [62]:

$$\sigma = C\Delta w \quad (25)$$

where  $\Delta w$  is the change in shift due to the applied load and  $C$  is a calibration constant which is the slope of the Raman shift vs stress curve. A stress map of the scanned area near the interface at different loads is shown in Fig. 7. The stress represents the local uniaxial tensile stress. A comprehensive study about the stress measurement in Raman spectroscopy is reported in [16]. The stress obtained from the Raman spectroscopy near the interface at the start of delamination is taken to be the interface strength. Due the circular boundary between HTPB and AP, the stress around this curved interface changes from maximum at 0° to the minimum at 90° from the loading direction. An average of the stress around the curved interface is taken to be the strength of the interface,  $T_{\max}^n = 2.91$  MPa.

The load displacement curve as shown in Fig. 8 is used to calculate the energy required for delamination. The area under the load displacement curve between the point where the crack reaches the AP-HTPB interface and the point where the delamination happens is the total energy required for the interface delamination. The cohesive fracture energy was then calculated by:

$$\Phi_0 = \frac{U}{A}, \quad (26)$$

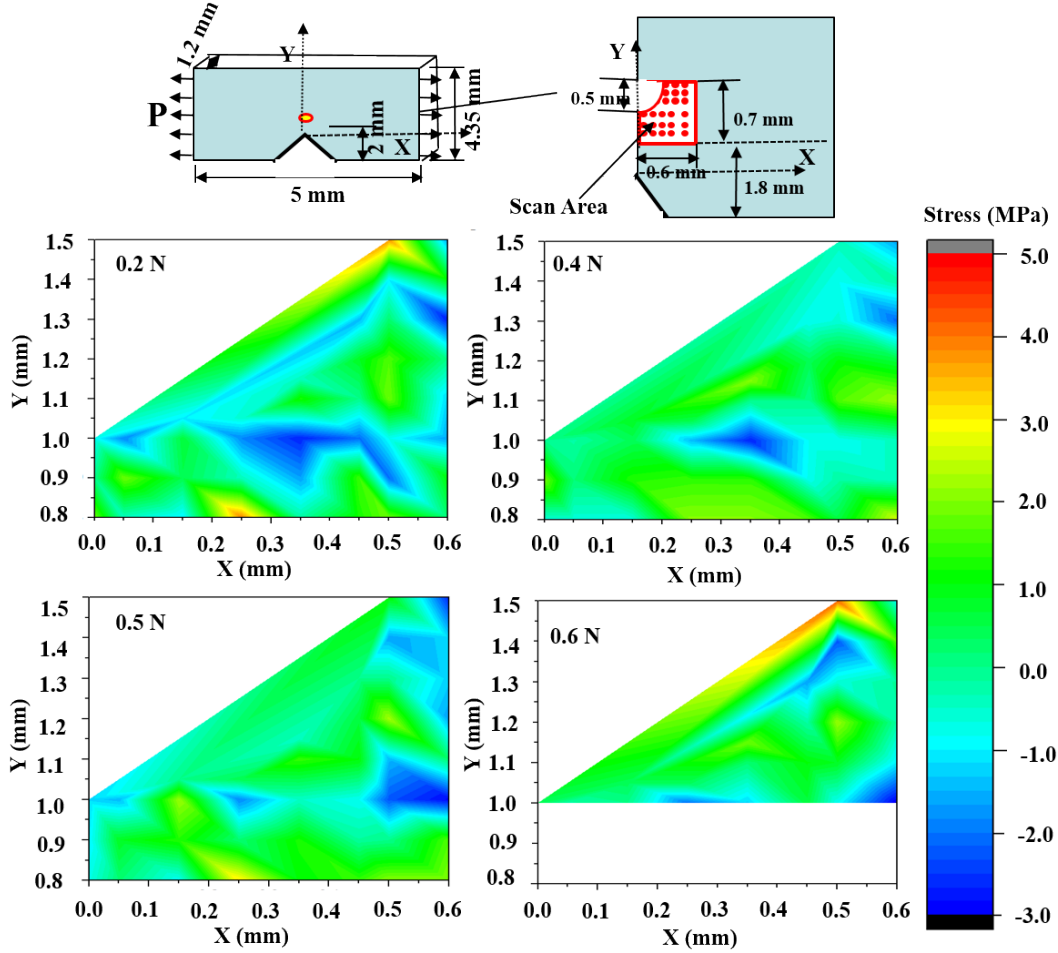


Figure 7: (a) Scanned area in Raman experiment. (b) Stress contour measured from Raman spectroscopy at different loads.

where  $U$  is the total energy required for delamination and  $A$  is the surface area created due to delamination. The total energy required for the delamination was calculated to be equal to 0.025 N-mm. Cohesive fracture energy was obtained using Eq. 26, and it is equal to 0.16 N/mm.

The stress-strain curve obtained from the nanoindentation experiment is shown in Fig. 9. The curve approximately follows a linear relation for strain 0.2~0.7. The slope of the stress-strain curve within this range is taken as the stiffness of the interface. The interface stiffness is obtained as  $\beta = 1,900$  MPa/mm. Therefore, the critical normal separation for the bilinear cohesive traction-separation relationship is derived as  $\Delta_{nc} = 2\Phi_0/T_{max}^n = 0.11$  mm. We note that Tan et al. [53] also obtained this value by measuring the opening displacement when the

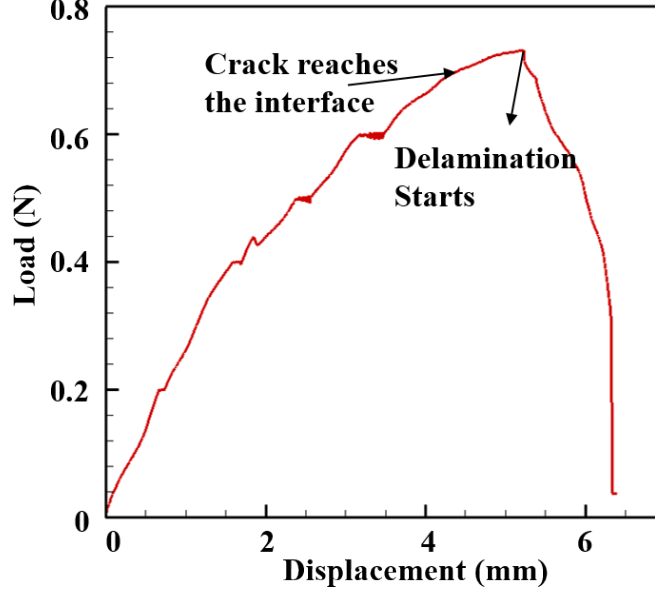


Figure 8: Load displacement curve measured in Raman experiment.

cohesive stress reaches zero in the fracture experiment of PBX 9501 composite. The elastic limit  $\eta_0$  is  $T_{max}^n / (\beta \Delta_{nc}) = 0.014$ . The tangential critical separation  $\Delta_{tc}$  is not directly obtained from the Raman experiment, since only the uniaxial tensile load test is conducted. The ratio of the critical normal and tangential separation  $\alpha$  is taken as 0.417, which has been used to study the interface failure of similar energetic composite material PBX 9501 by Wu and Huang [63].

In the current work, the penalty parameter is taken as the same as the cohesive stiffness, i.e.,  $\beta = 1,900$  MPa/mm. Further increase in the value of the penalty parameter reduces the time step size and increases the overall simulation time, without appreciable difference in the simulation results. This point has been verified using numerical simulations. In general, the friction coefficient depends on many factors, such as normal pressure, relative tangential velocity, surface roughness and temperature [61]. Dienes et al. [17] used the friction coefficient of 0.2 for the crack interfacial friction within PBX 9501, and is employed in the current study. The regularization parameter is introduced purely from the numerical efficiency point of view, therefore is determined by a numerical parametric study. Under the threshold that the error caused by this regularization is not greater than 0.2% compared to the classical Coulomb law,  $\varepsilon = 10^{-5}$  is numerically determined. The calibrated interface model parameters are

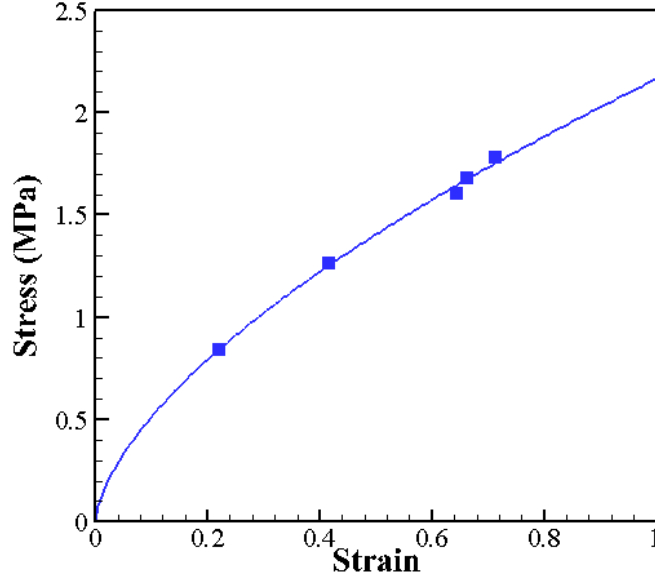


Figure 9: Interface stress-strain curve extracted from the nanoindentation experiment.

Table 2: Interface model parameters.

$T_{\max}^n$ [MPa]	$\eta_0$	$\Delta_{nc}$ [mm]	$\Delta_{tc}$ [mm]	$\beta$ [MPa/mm]
2.91	0.014	0.11	0.264	1900
$\mu_0$	$\varepsilon$	$w_{\text{int}}$ [mm]	$\rho_{\text{int}}$ [g/mm <sup>3</sup> ]	$C_{V\text{int}}$ [mJ/mm <sup>3</sup> K]
0.2	$10^{-5}$	$10^{-3}$	$1.45 \times 10^{-3}$	2.054

summarized in Table 2.

## 5 Results and Discussion

The calibrated models, along with the Kolsky bar experiments, were employed to study the dynamic behavior of AP-HTPB composite. The primary focus of the study is the assessment of failure at the particle/binder interface.

### 5.1 Kolsky bar experiment results

The setup of the Kolsky bar experiment is described in Section 2.4. The traces from a test on an AP-HTPB sample with 0.5 wt.% Tepanol is shown in Fig 10. The blue curve is the strain gauge output that shows the incident and reflected waves from the bar and the red

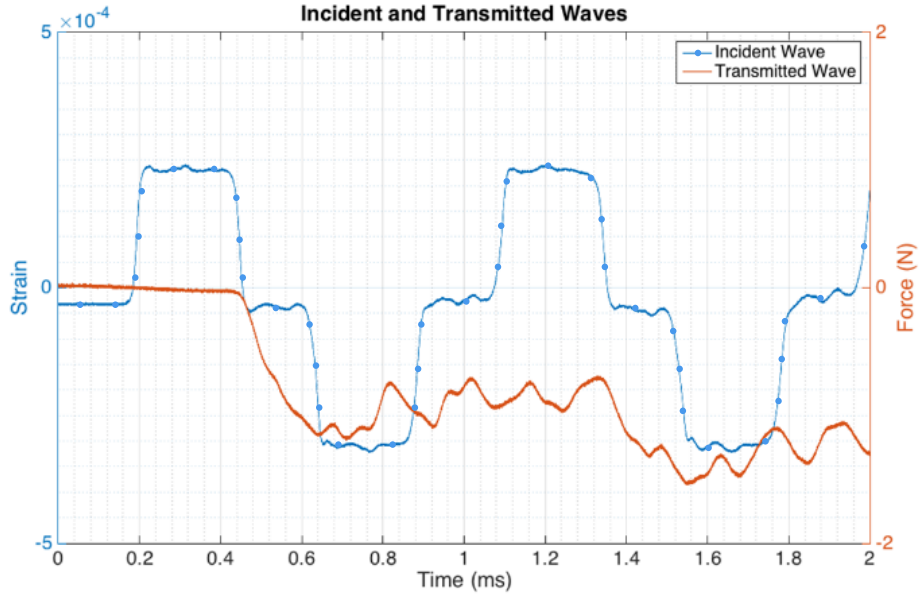


Figure 10: The measured strain and force (dynamic) in the Kolsky bar tension experiment.

curve shows the force reading from the load cell (transmitted wave). When the incident wave reaches the bar end, the deflection is transmitted to the sample at a rate of 3 m/s. The wave reflects multiple times across the bar, putting more tension on the sample as the whole bar moves away from the load cell. The corresponding phase contrast images in Fig. 11 show a displacement of  $600 \mu\text{m}$  at each step at the particle location. The onset of delamination occurs just as the third wave hits, which is outside the recorded oscilloscope window. However, the dynamic force can be estimated based on the force from the previous wave about 2 N. The sample was also pre-strained by 20% ( $600 \mu\text{m}$  extension over the 3 mm length) so that the delamination could be observed within the imaging window area. The load drop due to the static case is estimated to be about 1.5 N, so the delamination force is estimated as  $3.5 \pm 0.5$  N. The delamination starts at the trailing edge of the particle at about  $45^\circ$  symmetrically and extends towards the center forming a cone shaped void with increasing load. Figure 11 shows the delamination of the entire trailing edge surface between  $\pm 45^\circ$  at different stages.

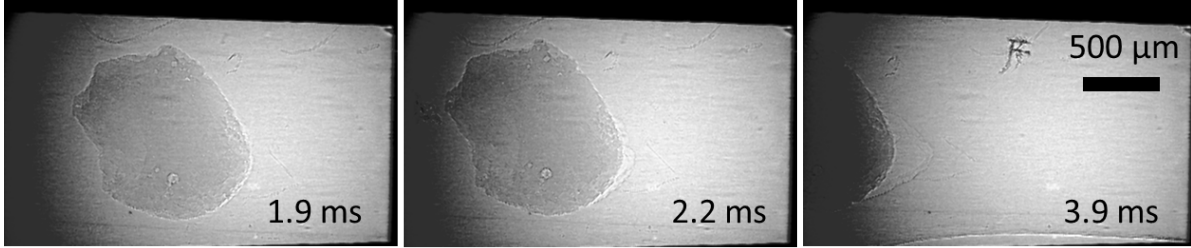


Figure 11: The stages of delamination of the trailing edge surface during the tension test. The stress concentration around the trailing edge initiates delamination, and the voids merge and grow into a cone with increasing load.

## 5.2 Kolsky bar simulation results

A two dimensional numerical simulation is carried out for the AP-HTPB specimen with a single AP particle embedded in HTPB binder to simulate the separation observed in the experiment. Figure 12 illustrates the geometry and boundary conditions employed in the numerical simulation. The length and width of the specimen is set to be  $L = 3\text{mm}$  and  $W = 2\text{mm}$ , respectively. The AP particle is idealized as a circle with diameter  $D = 1\text{mm}$ . While the particle geometry in the experiment deviates from this approximation, the region of initial debonding observed in the experiments do not contain observable stress concentrations due to irregular shape. In the Kolsky bar tension test, the load is incident tensile pulse followed by repeated reflected strain wave. Dispersion effects lead to wave form distortion and attenuation. Thus the wave form typically has oscillatory noise with gradually decreasing amplitude. The loading condition in the Kolsky bar tension test is idealized as the step-wise-increasing displacement. The right boundary of the numerical specimen is constrained and the displacement load is applied at the left end. The top and bottom boundaries are traction free. Pre-straining in the experiment is simulated by a quasi-static loading step prior to the onset of high rate loading. All the material properties and model parameters used in the simulation are provided in the previous section.

Mesh sensitivity study is performed to ensure that further refinement of mesh does not significantly affect the results. A ramp load with the period of 0.8 ms without pre-loading under the same loading rate as the first ramp as shown in the loading profile in Fig. 12, i.e., 1000/s, is used to investigate the mesh effects on the stress and the initiation of debonding. In

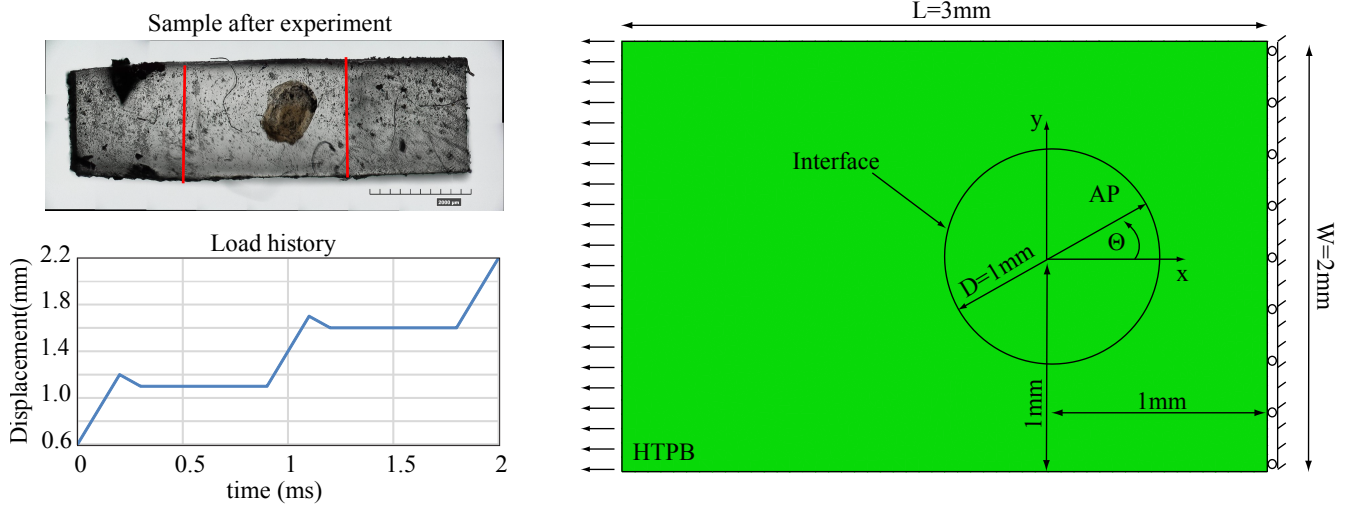


Figure 12: Kolsky bar simulation model setup.

Fig. 13, the maximum normal stress  $S_{11}$  around the particle and the separation initiation time as a function the number of elements is shown. In the current work, 11,420 triangular elements are used for phase material (HTPB and AP) with 100 cohesive zone elements embedded along the interface, which show very similar response compared to further refined models.

The reaction force computed at the right boundary of the specimen is plotted along with the force measured at the load cell in the Kolsky bar experiment in Fig. 14. During the pre-straining stage, the static reaction force at 20% pre-strain is 1.5 N. At the first load peak at  $t = 0.2$  ms, the force measured in the experiment is approximately 2.6 N compared to the reaction force computed in the simulation of 2.4 N. Further increase in the applied displacement to 1.7 mm at  $t = 1.1$  ms, the experiment shows the second peak with magnitude 3.1 N, while the simulation predicts 2.7 N reaction force. In the intermediate stage between the two ramp loads, oscillatory reaction is observed both in the experiment and the model with approximately the same frequency. The magnitude of the response tends to decrease due to the material dissipation. X-ray synchrotron imaging indicates that the debonding in normal direction ( $\Theta=0^\circ$  in Fig. 12) in the specimen occurs at  $t = 1.9$  ms. The reaction force is not measured at this point in experiment. The model prediction is 2.9 N. The reaction force computed in numerical simulation shows an overall agreement with the force measured in the experiment. The force amplitude is under-predicted by 0.2 N in the dynamic loading process

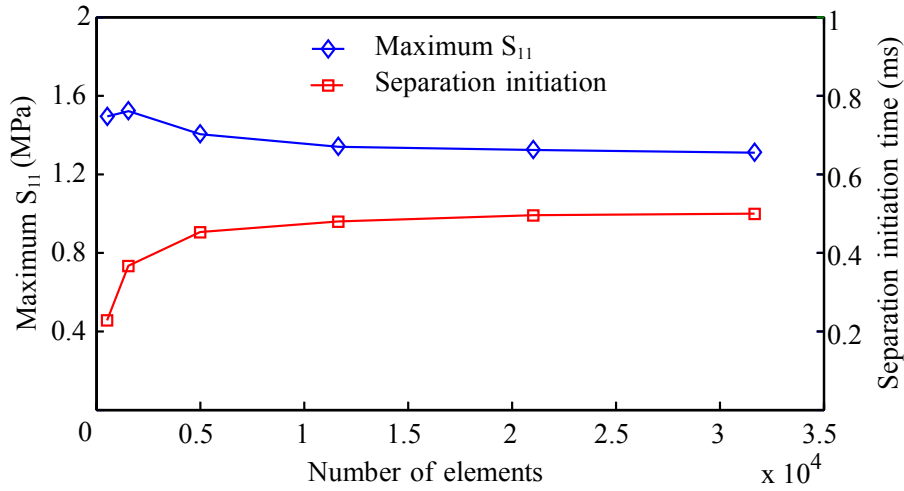


Figure 13: Variation of maximum normal stress  $S_{11}$  and the interface separation initiation time around the particle as a function of discretization.

despite the match in the static pre-straining. This is mainly caused by the uncertainty in the HTPB viscoelastic properties. The calibrated viscoelastic material parameters based on the data available in literature is an approximation due to potential differences in the HTPB composition.

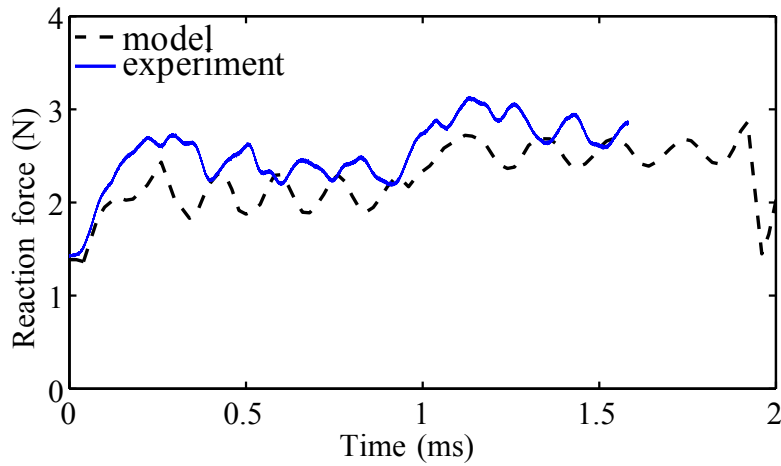


Figure 14: Reaction force history as computed by the model and observed in the experiment.

Figure 15 shows experimentally observed deformed state of the specimen during the loading process, compared with stress contours from the simulation at four time instances:  $t = 1.0$  ms,  $t = 1.2$  ms,  $t = 1.7$  ms,  $t = 1.92$  ms. In the first stage of loading ( $0 \leq t \leq 0.9$  ms), the particle and binder remains fully bonded and the composite deforms viscoelastically. The maximum

stress of 2.2 MPa occurs at the particle binder interface at  $t = 1.0$  ms without any debonding. At  $t = 1.2$  ms, the interface debonding initiates and is observable in both the experiment and the simulation. The debonding initiates at a small interface region at an angle of  $\Theta = -45^\circ$  (see Fig. 12) first in the experiment while the remainder of the interface remains fully bonded. In the simulation, we observe that the debonding simultaneously initiates at  $\pm 45^\circ$  and  $\pm 135^\circ$  due to the symmetry of the geometry. In contrast, irregular particle shape allows the initiation of debonding to occur at a single site. These debonding initiation locations correspond to where the shear stress and consequently tangential tractions are maximum, as is shown in Fig. 16. The initiation of debonding in shear at  $\pm 45^\circ$  is attributed to the lower shear cohesive strength at the interface compared to the normal cohesive strength. At  $t=1.2$ ms, the local maximum normal stress around the particle occurs at  $0^\circ$ , but is less than the normal cohesive strength,  $T_{max}^n$ . In contrast, the maximum local shear stress at  $\pm 45^\circ$  (Fig. 16) reaches the shear cohesive strength,  $T_{max}^t$ . It is important to note that direct experimental data for the shear cohesive strength parameter is not available. The close match between experimental observation and the simulation in Fig. 15 points to the plausibility of the value of the shear cohesive strength parameter used in the simulation.

At  $1.2 \leq t \leq 1.8$  ms, the specimen undergoes a relatively constant strain state along with a slight oscillation due to propagation stress waves as demonstrated by the reaction force oscillations in Fig. 14. A slight increase of interfacial damage, is observed in the experiment with the second shear dominated separation site observable at  $t=1.7$  ms. Failure initiation sites remain consistent between the experimental and simulated results. Further increase in loading (after  $t=1.7$  ms) leads to extensive debonding in the specimen. The cracks along interface at  $\pm 45^\circ$  (shear dominated) and  $0^\circ$  (normal dominated) rapidly extend and coalesce, resulting in debonding of the entire interface region  $-45^\circ \leq \Theta \leq 45^\circ$  and rapidly propagating around the interface thereafter. When this happens, the reaction force dramatically drops, as shown in Fig. 14.

The interface separation as measured in the experiment and predicted by the simulation at  $\pm 45^\circ$  is shown in Fig. 17. The onset of separation is progressive in both experiment and simulation within  $1 \leq t \leq 1.2$  ms time window. The separation magnitude predicted in the

simulation is close to experimentally observed value for  $\Theta = -45^\circ$ . When  $1.2 \leq t \leq 1.7$  ms, where the load profile is a plateau, the predicted separation is approximately constant, yet the separation observed in the experiment slightly increases. This observation points to a viscous debonding process not considered in the current formulation. The final extent of separation at the debonding site predicted by the simulation is larger than the experimentally observed value. This is due to the 2-D representation of the simulated specimen compared to the experiment, where the particle is fully embedded in the binder and constrained from excessive separation by binder at the out-of-plane direction.

In the simulation, the maximum temperature rise occurs at the left boundary where the load is applied,  $\Delta T = 0.1^\circ\text{K}$ . The maximum temperature rise around the particle is  $0.08^\circ\text{K}$ . The thermal effects in this loading profile is therefore negligible.

### 5.3 Sensitivity to interfacial strength and energy

Due to the stochasticity existing in the material system and the uncertainty in experiments and the simulation, the interface properties might be a distribution (e.g. normal or logarithmic normal) instead of a deterministic value. The sensitivity analysis is provided to investigate the model response as a function of different interface properties. The analysis is performed for a range of cohesive strengths and cohesive fracture energies with the same model setup (see Fig. 12). A comprehensive parametric study about the cohesive zone models is presented in [28]. In the sensitivity analysis, only the single quantity of interest (i.e., cohesive strength or cohesive fracture energy) is varied, while all other parameters are kept the same as summarized in Table 2.

Figure 18(a) shows the time instances that interface separation initiation and full separation occur for a range of cohesive strength. For  $1.7 \leq T_{\max}^n \leq 2.2$  MPa, both separation initiation and full separation occur within the first ramp period (i.e.  $0 \leq t \leq 0.2$  ms). Further increase the cohesive strength up to 2.8 MPa, while the interface debonding still initiates within the first ramp, full separation does not occur until the load is in the second ramp. When  $3.0 \leq T_{\max}^n \leq 3.5$ , the separation initiation occurs in the second ramp and the full separation happens in the third ramp. As the cohesive strength further increases, the interface starts to debond

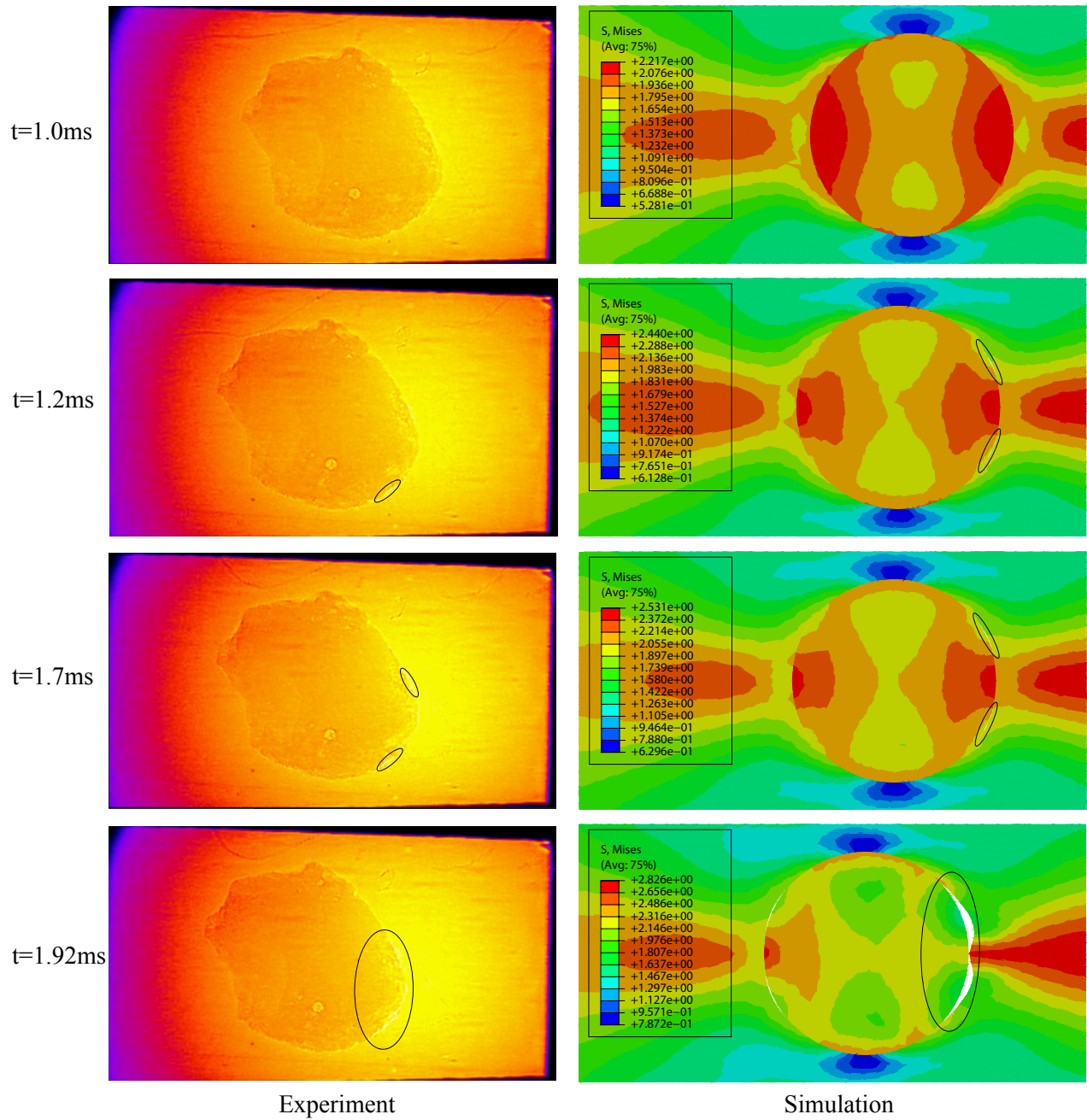


Figure 15: Interface separation evolution as a function of time in the experiment and the simulation.

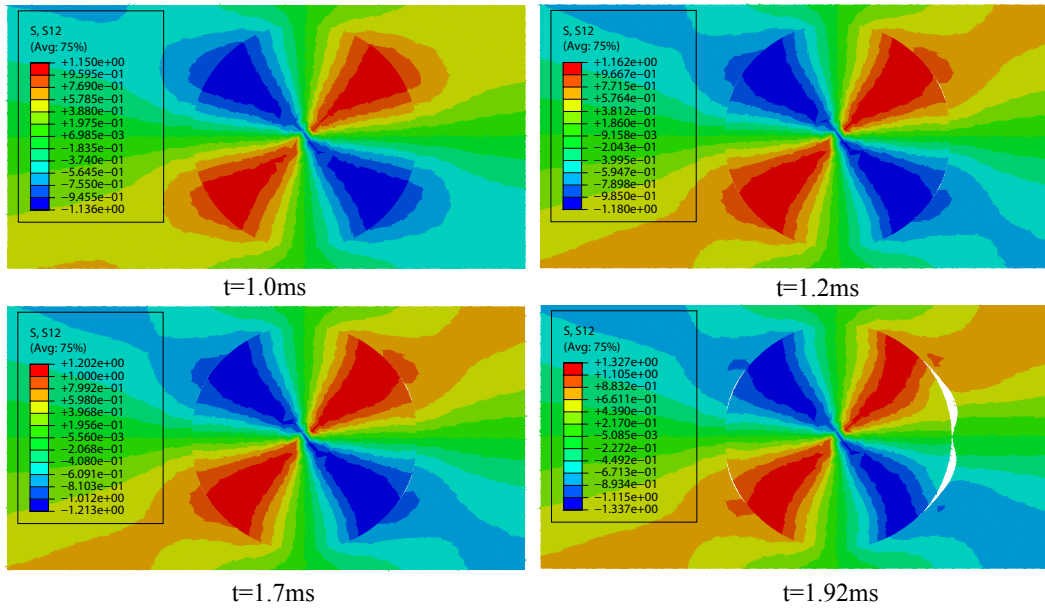


Figure 16: Simulated local shear stress  $S_{12}$  in cylindrical coordinate system with its origin at the center of the particle at different time instances.

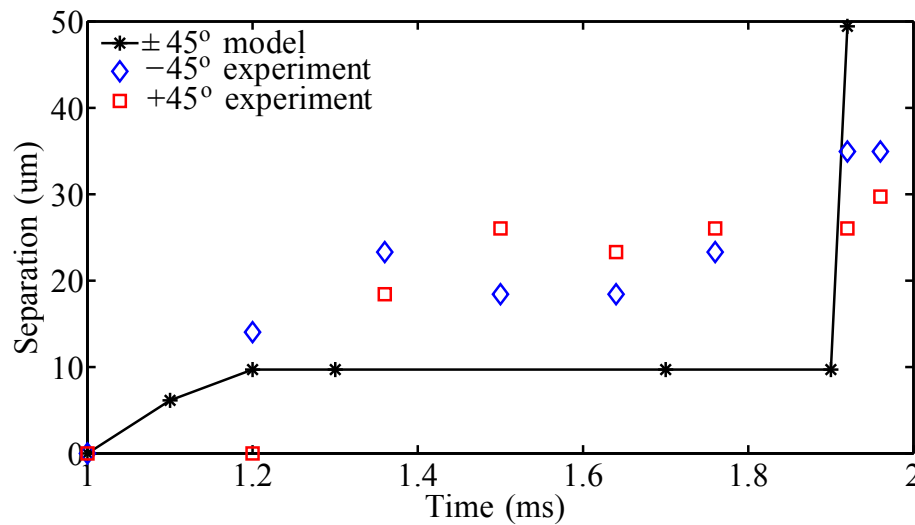


Figure 17: Evolution of interface separation as measured from experiments and predicted by the model.

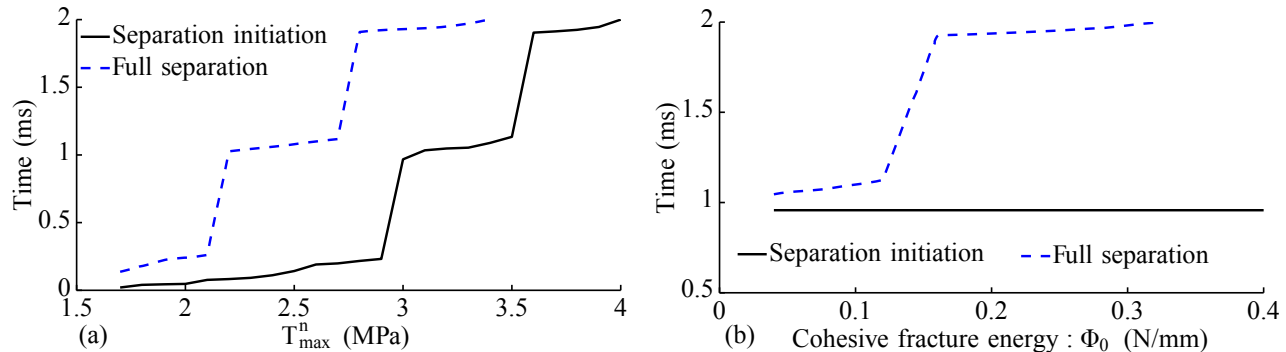


Figure 18: Sensitivity of interface separation with respect to: (a) cohesive strength, (b) cohesive fracture energy.

in the third ramp and no full debonding is observed in the simulation.

The separation initiation is not sensitive to the cohesive fracture energy. It is invariant as the cohesive fracture energy increases, as shown in Fig. 18(b). Once the debonding initiates, cohesive fracture energy controls the progressive failure of interface. As the cohesive fracture energy increases, the full separation time instance monotonically increases. This trend continues up to  $\Phi_0 = 0.32$  N/mm, where full separation does not occur in the loading process.

## 5.4 Ultrasonic vibration simulation

A numerical study is performed to investigate the thermo-mechanical behavior of a single particle AP-HTPB specimen under ultrasonic vibration. The simulation setup is shown in Fig. 19. Sinusoidal horizontal displacement load with 40 kHz frequency and 10  $\mu\text{m}$  amplitude, along with a 10 mN static pressure applied at the top surface of the specimen within 0.5 mm distance. The AP particle is placed 0.5 mm from the top surface immediately below the loading. Two simulations are conducted to study the relative significance of the viscoelastic dissipation induced heating within the binder and the frictional heating at particle/binder interface. Simulation I is performed with interface fully bonded and remains fully bonded throughout the vibrational load. In simulation II, the specimen is subjected to a single pre-straining overload cycle of 0.8 mm maximum amplitude within 1.6 ms. The initial overload creates interface debonding as shown in Fig. 20, prior to the application of the vibrational

load. Both simulations are conducted at initial temperature of 296°K.

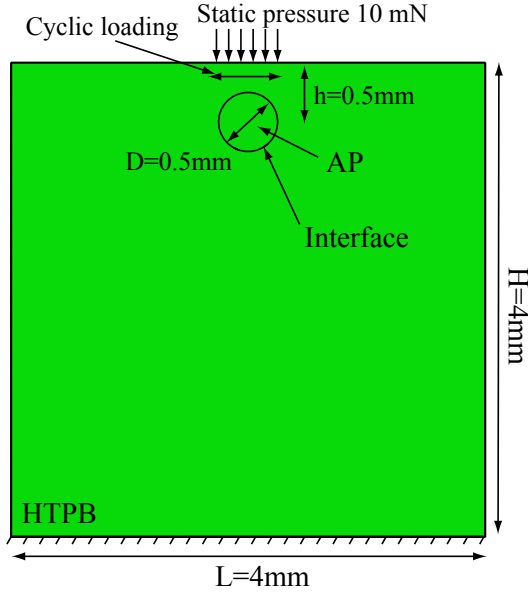


Figure 19: Ultrasonic vibration simulation model setup.

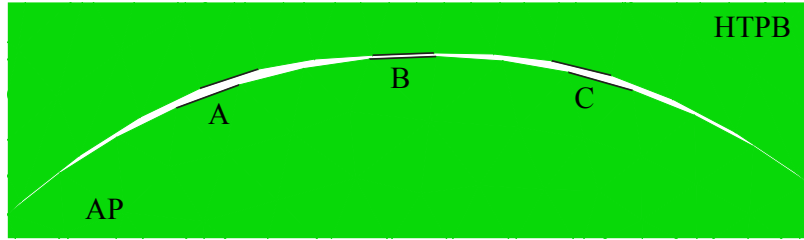


Figure 20: The top surface of the AP particle after pre-straining.

The temperature rise at three locations (A, B and C in Fig. 20) are probed for both simulations. The damage at the three locations during the pre-straining are:  $d_A = 0.736$ ,  $d_B = 0$  and  $d_C = 0.675$  for simulation II, while simulation I does not have damage at the same locations. Figure 21 shows the temperature contour at  $t=100$  ms for both simulations. An overall similar temperature distribution is observed, where the maximum temperature rise within HTPB occurs at the area on top of the particle, due to stress concentration.

Figure 22 shows the temperature rise  $\Delta T$  within HTPB near the locations A, B and C for simulation I (without debonding) and simulation II (with debonding). While the temperature monotonically increase as a function of time for both simulations, simulation II displays a lower temperature change at locations A and C, but higher temperature change at location

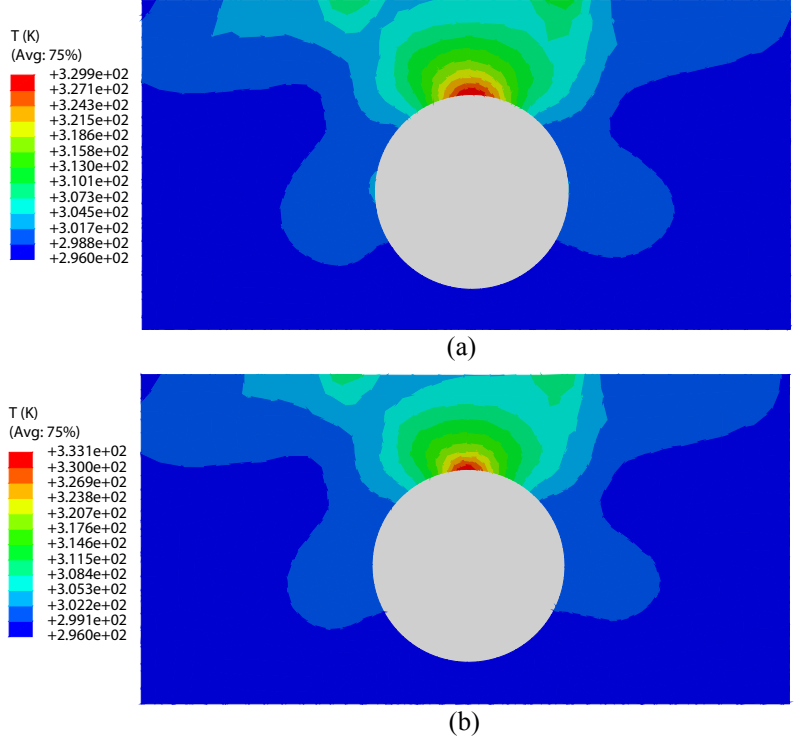


Figure 21: Temperature contour within HTPB binder at  $t=100$  ms. (a) Simulation I, (b) Simulation II.

B compared to simulation I over the entire time history. This is because interface damage at locations A and C leads to reduced local stresses, which in turn intensifies the stress at the undamaged area (e.g. location B) and further increases the local temperature. This observation indicates that damage at the interface affects not only the heating at the interface, but also the viscoelastic dissipation induced heating within the HTPB binder near the interface, by changing the local stress distribution. The maximum rate of change in temperature computed from the simulation without interface debonding (simulation I) is  $350^\circ \text{C/s}$  and with interface debonding (simulation II) is  $390^\circ \text{C/s}$ , respectively.

The interface heating at interface locations A and C computed within the cohesive zone elements are shown in Fig. 23. The temperature rise at location B is zero, since  $d_B = 0$  and the interface separation is in Stage-I (see Fig. 3). The rate of temperature rise is  $0.11^\circ \text{C/s}$  and  $0.09^\circ \text{C/s}$ , for locations A and C, respectively, with gradually decreasing rates due to the softening of adjacent HTPB at elevated temperature. Compared to the temperature rise rate within HTPB, the interface friction induced temperature rise occurs at a much lower rate

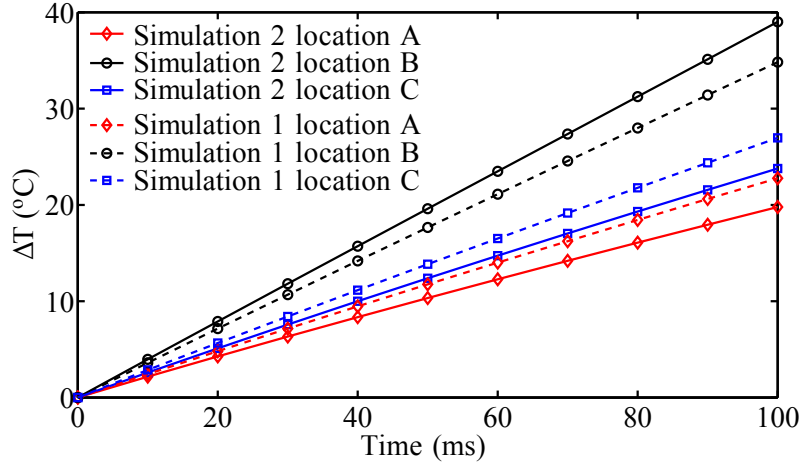


Figure 22: Temperature rise history at location A, B and C within HTPB for simulation I and simulation II.

under the current simulation setup.

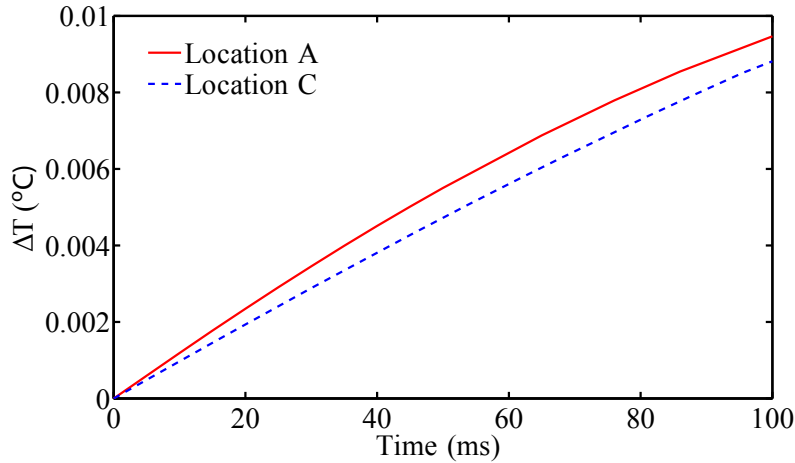


Figure 23: Interface temperature rise due to frictional heating.

## 6 Conclusion and future work

A combined computational-experimental study of the mesoscale thermo-mechanical behavior of AP-HTPB composite energetic material under dynamic loading conditions is presented. The study considered the thermo-mechanical models of the composite constituents, which are carefully calibrated and validated against a range of experiments. To the best authors' knowledge, this is the first experimentally calibrated and validated model for AP-HTPB energetic

material subjected to dynamic loading.

The observations from the experiments and simulations include: (1) the debonding of the circular AP particle and HTPB binder initiates in a shear dominated manner; (2) the interface strength plays an important role in both separation initiation and full separation, while the response is relatively less sensitive to the cohesive fracture energy under the unidirectional high-rate loading; (3) the viscoelastic dissipation intensified around the interface has a higher contribution to heating compared to the frictional heating at particle/binder interface under vibration conditions.

Future investigations will continue to address several issues. First, the characterization of the interface properties as a function of temperature and rate are critical to achieving a predictive modeling capability of such energetic composites under dynamic loading. Combined experimental-computational studies are necessary to address these dependencies. Second, the quantification of uncertainties in the material constituent, (i.e., interface, particle and binder) thermo-mechanical properties, particle geometry and morphology are important factors towards application to the realistic energetic material systems, with large volume fraction of particles and variable particle morphologies. Third, to enable computational simulation of realistic size problems, multiscale models that can account for the dissipative and dispersive behavior in high dynamic conditions [26, 27] need to be developed, along with reduced order modeling [40, 67, 66, 38, 39] for high computational efficiency.

## Acknowledgment

The authors gratefully acknowledge the financial support from the Air Force Office of Scientific Research, Dynamic materials and Interactions program (Grant No.: FA9550-15-1-0202, Program Manager: Dr. Jennifer Jordan). We thank Prof. Weinong Chen of Purdue University for allowing the use of his Kolsky bar setup at Argonne National Laboratory. We also thank Kamel Fezzaa, Tao Sun, Niranjana Parab, Jesus Mares and Zane Roberts for helping with the Kolsky bar experiment.

## References

- [1] R. K. A. Al-Rub and G. Z. Voyiadjis. A finite strain plastic-damage model for high velocity impact using combined viscosity and gradient localization limiters: Part i-theoretical formulation. *Int. J. Damage Mech.*, 15(4):293–334, 2006.
- [2] A. V. Amirkhizi, J. Isaacs, J. McGee, and S. Nemat-Nasser. An experimentally-based viscoelastic constitutive model for polyurea, including pressure and temperature effects. *Philos. Mag.*, 86(36):5847–5866, 2006.
- [3] E. Anastassakis, A. Pinczuk, E. Burstein, F. H. Pollak, and M. Cardona. Effect of static uniaxial stress on the raman spectrum of silicon. *Solid State Commun.*, 8(2):133–138, 1970.
- [4] R. W. Armstrong, C. S. Coffey, and W. L. Elban. Adiabatic heating at a dislocation pile-up avalanche. *Acta Metall.*, 30(12):2111–2116, 1982.
- [5] R. W. Armstrong, C. S. Coffey, V. F. DeVost, and W. L. Elban. Crystal size dependence for impact initiation of cyclotrimethylenetrinitramine explosive. *J. Appl. Phys.*, 68(3):979–984, 1990.
- [6] R. W. Armstrong, H. L. Ammon, W. L. Elban, and D. H. Tsai. Investigation of hot spot characteristics in energetic crystals. *Thermochim. Acta*, 384(1):303–313, 2002.
- [7] M. R. Baer. Modeling heterogeneous energetic materials at the mesoscale. *Thermochim. Acta*, 384(1):351–367, 2002.
- [8] J. E. Balzer, C. R. Siviour, S. M. Walley, W. G. Proud, and J. E. Field. Behaviour of ammonium perchlorate-based propellants and a polymer-bonded explosive under impact loading. *Proc. R. Soc. Lond. A*, 460(2043):781–806, 2004.
- [9] N. R. Barton, N. W. Winter, and J. E. Reaugh. Defect evolution and pore collapse in crystalline energetic materials. *Modell. Simul. Mater. Sci. Eng.*, 17(3):035003, 2009.

- [10] A. Barua and M. Zhou. A lagrangian framework for analyzing microstructural level response of polymer-bonded explosives. *Modell. Simul. Mater. Sci. Eng.*, 19(5):055001, 2011.
- [11] A. Barua, Y. Horie, and M. Zhou. Microstructural level response of hmx–estane polymer-bonded explosive under effects of transient stress waves. *Proc. R. Soc. Lond. A*, 468(2147):3725–3744, 2012.
- [12] T. B. Brill and F. Caetz. Laser Raman studies of solid oxidizer behavior. *14th Aerospace Sciences Meeting*, pages 1–7, 1976.
- [13] M. Buback and K. R. Schulz. Raman scattering of pure ammonia at high pressures and temperatures. *J. Phys. Chem.*, 80(22):2478–2482, 1976.
- [14] C. M. Cady, W. R. Blumenthal, G. T. Gray, and D. J. Idar. Mechanical properties of plastic-bonded explosive binder materials as a function of strain-rate and temperature. *Polym. Eng. Sci.*, 46:812–819, 2006.
- [15] T. Chakraborty, S. S. Khatri, and A. L. Verma. Temperature-dependent raman study of ammonium perchlorate single crystals: The orientational dynamics of the  $\text{nh}^+ 4$  ions and phase transitions. *J. Chem. Phys.*, 84(12):7018–7027, 1986.
- [16] I. De Wolf. Micro-raman spectroscopy to study local mechanical stress in silicon integrated circuits. *Semicond. Sci. Technol.*, 11(2):139, 1996.
- [17] J. K. Dienes, Q. H. Zuo, and J. D. Kershner. Impact initiation of explosives and propellants via statistical crack mechanics. *J. Mech. Phys. Solids*, 54(6):1237–1275, 2006.
- [18] R. Duddu and H. Waisman. A temperature dependent creep damage model for polycrystalline ice. *Mech. Mater.*, 46:23–41, 2012.
- [19] N. F. Fell, J. M. Widder, S. V. Medlin, J. B. Morris, and R. A. Pesce-Rodriguez. Fourier transform raman (ftr) spectroscopy of some energetic materials and propellant formulations ii. Technical report, DTIC Document, 1995.

- [20] J. E. Field. Hot spot ignition mechanisms for explosives. *Acc. Chem. Res.*, 25(11):489–496, 1992.
- [21] G. T. Gray III, W. R. Blumenthal, D. J. Idar, and C. M. Cady. Influence of temperature on the high-strain-rate mechanical behavior of pbx 9501. In *The tenth American Physical Society topical conference on shock compression of condensed matter*, volume 429, pages 583–586, 1998.
- [22] B. Han, Y. Ju, and C. Zhou. Simulation of crack propagation in htpb propellant using cohesive zone model. *Eng. Fail. Anal.*, 26:304–317, 2012.
- [23] Donna M. Hanson P. and T. P. Parr. Thermal properties measurements of solid rocket propellant oxidizers and binder materials as a function of temperature. *J. Energetic Mater.*, 17(1):1–48, 1999.
- [24] M. Hudspeth, B. Claus, N. Parab, B. Lim, W. Chen, T. Sun, and K. Fezza. In situ visual observation of fracture processes in several high-performance fibers. *Journal of Dynamic Behavior of Materials*, 1(1):55–64, 2015.
- [25] T. Hui and C. Oskay. Computational modeling of polyurea-coated composites subjected to blast loads. *J. Compos. Mater.*, 46:2167–2178, 2012.
- [26] T. Hui and C. Oskay. A high order homogenization model for transient dynamics of heterogeneous media including micro-inertia effects. *Comput. Methods Appl. Mech. Eng.*, 273:181–203, 2014.
- [27] T. Hui and C. Oskay. Laplace-domain, high-order homogenization for transient dynamic response of viscoelastic composites. *Int. J. Numer. Methods Eng.*, 103(13):937–957, 2015.
- [28] S. Jimenez and R. Duddu. On the parametric sensitivity of cohesive zone models for high-cycle fatigue delamination of composites. *Int. J. Solids Struct.*, 2015.
- [29] Y. Lin, W. L. Mao, V. Drozd, J. Chen, and L. L. Daemen. Raman spectroscopy study of ammonia borane at high pressure. *J. Chem. Phys.*, 129(23):234509, 2008.

- [30] D. A. Lucca, M. J. Klopstein, O. R. Mejia, L. Rossetini, and L. T. DeLuca. Investigation of ammonium perchlorate by nanoindentation. *Mater. Sci. Technol.*, 22(4):396–401, 2006.
- [31] J. O. Mares, J. K. Miller, N. D. Sharp, D. S. Moore, D. E. Adams, L. J. Groven, J. F. Rhoads, and S. F. Son. Thermal and mechanical response of pbx 9501 under contact excitation. *J. Appl. Phys.*, 113(8):084904, 2013.
- [32] J. O. Mares, J. K. Miller, I. E. Gunduz, J. F. Rhoads, and S. F. Son. Heat generation in an elastic binder system with embedded discrete energetic particles due to high-frequency, periodic mechanical excitation. *J. Appl. Phys.*, 116(20):204902, 2014.
- [33] E. M. Mas, B. E. Clements, W. R. Blumenthal, C. M. Cady, G. T. Gray, and C Liu. A viscoelastic model for pbx binders. In *AIP Conference Proceedings*, number 1, pages 661–664, 2002.
- [34] R. Menikoff and T. D. Sewell. Constituent properties of hmx needed for mesoscale simulations. *Combust. Theor. Model.*, 6(1):103–125, 2002.
- [35] J. K. Miller, J. O. Mares, I. E. Gunduz, S. F. Son, and J. F. Rhoads. The impact of crystal morphology on the thermal responses of ultrasonically-excited energetic materials. *J. Appl. Phys.*, 119(2):024903, 2016.
- [36] P Nallasamy, P.M. Anbarasan, and S. Mohan. Vibrational Spectra and Assignments of cis- and Trans-1,4- Polybutadiene. *Turk J Chem*, 26:105–111, 2002.
- [37] S. Ninet, F. Datchi, A. M. Saitta, M. Lazzeri, and B. Canny. Raman spectrum of ammonia IV. *Phys. Rev. B*, 74(10):104101, sep 2006.
- [38] C. Oskay. Two-level multiscale enrichment methodology for modeling of heterogeneous plates. *Int. J. Numer. Methods Eng.*, 80(9):1143, 2009.
- [39] C. Oskay. Variational multiscale enrichment method with mixed boundary conditions for modeling diffusion and deformation problems. *Comput. Methods Appl. Mech. Eng.*, 264: 178–190, 2013.

- [40] C. Oskay and J. Fish. Eigendeformation-based reduced order homogenization for failure analysis of heterogeneous materials. *Comput. Methods Appl. Mech. Eng.*, 196:1216–1243, 2007.
- [41] N. D. Parab, J. T Black, B. Claus, M. Hudspeth, J. Sun, K. Fezzaa, and W. W. Chen. Observation of crack propagation in glass using x-ray phase contrast imaging. *Int. J. Appl. Glass Sci.*, 5(4):363–373, 2014.
- [42] K. Park and G. H. Paulino. Computational implementation of the ppr potential-based cohesive model in abaqus: educational perspective. *Eng. Fract. Mech.*, 93:239–262, 2012.
- [43] S. M. Peiris, G. I. Pangilinan, and T. P. Russell. Structural properties of ammonium perchlorate compressed to 5.6 gpa. *J. Phys. Chem. A*, 104(47):11188–11193, 2000.
- [44] P. J. Rae, H. T. Goldrein, S. J. P. Palmer, J. E. Field, and A. L. Lewis. Quasi-static studies of the deformation and failure of  $\beta$ -hmx based polymer bonded explosives. *Proc. R. Soc. Lond. A*, 458(2019):743–762, 2002.
- [45] P. J. Rae, S. J. P. Palmer, H. T. Goldrein, J. E. Field, and A. L. Lewis. Quasi-static studies of the deformation and failure of pbx 9501. *Proc. R. Soc. Lond. A*, 458(2025):2227–2242, 2002.
- [46] J. Renshaw, J. C Chen, S. D. Holland, and R. B. Thompson. The sources of heat generation in vibrothermography. *NDT and E Int.*, 44(8):736–739, 2011.
- [47] O. Samudrala, Y. Huang, and A. J. Rosakis. Subsonic and intersonic mode ii crack propagation with a rate-dependent cohesive zone. *J. Mech. Phys. Solids*, 50(6):1231–1268, 2002.
- [48] F. Schneider, T. Fellner, J. Wilde, and U. Wallrabe. Mechanical properties of silicones for mems. *J. Micromech. Microeng.*, 18(6):065008, 2008.
- [49] J. C. Simo and T. J.R. Hughes. *Computational inelasticity*. Springer Science & Business Media, 2006.

- [50] C. R. Siviour, M. J. Gifford, S. M. Walley, W. G. Proud, and J. E. Field. Particle size effects on the mechanical properties of a polymer bonded explosive. *J. Mater. Sci.*, 39(4): 1255–1258, 2004.
- [51] C. R. Siviour, P. R. Laity, W. G. Proud, J. E. F., D. Porter, P. D. Church, P. Gould, and W. Huntingdon-Thresher. High strain rate properties of a polymer-bonded sugar: their dependence on applied and internal constraints. *Proc. R. Soc. Lond. A*, 464(2093): 1229–1255, 2008.
- [52] V. Studer, G. Hang, A. Pandolfi, M. Ortiz, W. F. Anderson, and S. R. Quake. Scaling properties of a low-actuation pressure microfluidic valve. *J. Appl. Phys.*, 95(1):393–398, 2004.
- [53] H. Tan, C. Liu, Y. Huang, and P. H. Geubelle. The cohesive law for the particle/matrix interfaces in high explosives. *J. Mech. Phys. Solids*, 53(8):1892–1917, 2005.
- [54] V. Tomar, J. Zhai, and M. Zhou. Bounds for element size in a variable stiffness cohesive finite element model. *Int. J. Numer. Methods Eng.*, 61(11):1894–1920, 2004.
- [55] V. Tvergaard and J. W. Hutchinson. The influence of plasticity on mixed mode interface toughness. *J. Mech. Phys. Solids*, 41(6):1119–1135, 1993.
- [56] D. Verma and V. Tomar. An investigation into environment dependent nanomechanical properties of shallow water shrimp (pandalus platyceros) exoskeleton. *Mater. Sci. Eng., C*, 44:371–379, 2014.
- [57] D. Verma and V. Tomar. Strain rate dependent failure of metallic interfaces at nano-microscale via nanoimpact experiments. *20th International Conference on Composite Materials*, July 2015.
- [58] D. Verma and V. Tomar. A comparison of nanoindentation creep deformation characteristics of hydrothermal vent shrimp (rimicaris exoculata) and shallow water shrimp (pandalus platyceros) exoskeletons. *J. Mater. Res.*, 30(08):1110–1120, 2015.

- [59] D. Verma, T. Qu, and V. Tomar. Scale dependence of the mechanical properties and microstructure of crustaceans thin films as biomimetic materials. *JOM*, 67(4):858–866, 2015.
- [60] J. M. Winey, Y. A. Gruzdkov, Z. A. Dreger, B. J. Jensen, and Y. M. Gupta. Thermomechanical model and temperature measurements for shocked ammonium perchlorate single crystals. *J. Appl. Phys.*, 91(9):5650–5656, 2002.
- [61] P. Wriggers and T. A. Laursen. *Computational contact mechanics*, volume 30167. Springer, 2006.
- [62] X. Wu, J. Yu, T. Ren, and L. Liu. Micro-raman spectroscopy measurement of stress in silicon. *Microelectron. J.*, 38(1):87–90, 2007.
- [63] Y. Q. Wu and F. L. Huang. A micromechanical model for predicting combined damage of particles and interface debonding in pbx explosives. *Mech. Mater.*, 41(1):27–47, 2009.
- [64] J. Xu, X. Chen, H. Wang, J. Zheng, and C. Zhou. Thermo-damage-viscoelastic constitutive model of htpb composite propellant. *Int. J. Solids Struct.*, 51(18):3209–3217, 2014.
- [65] J. Zhai, V. Tomar, and M. Zhou. Micromechanical simulation of dynamic fracture using the cohesive finite element method. *J. Eng. Mater. Technol.*, 126(2):179–191, 2004.
- [66] S. Zhang and C. Oskay. Reduced order variational multiscale enrichment method for elasto-viscoplastic problems. *Comput. Methods Appl. Mech. Eng.*, 300:199–224, 2016.
- [67] X. Zhang and C. Oskay. Eigenstrain based reduced order homogenization for polycrystalline materials. *Comput. Methods Appl. Mech. Eng.*, 297:408–436, 2015.
- [68] F. Zhou, J. F. Molinari, and T. Shioya. A rate-dependent cohesive model for simulating dynamic crack propagation in brittle materials. *Eng. Fract. Mech.*, 72(9):1383–1410, 2005.

- [69] Z. Zhou, P. Chen, F. Huang, and S. Liu. Experimental study on the micromechanical behavior of a pbx simulant using sem and digital image correlation method. *Opt. Lasers Eng.*, 49(3):366–370, 2011.
- [70] Y. Zhu, K. M Liechti, and K. Ravi-Chandar. Direct extraction of rate-dependent traction–separation laws for polyurea/steel interfaces. *Int. J. Solids Struct.*, 46(1):31–51, 2009.